Available online at www.sciencedirect.com
ScienceDirect
Trans. Nonferrous Met. Soc. China 32(2022) 801−811
Transactions of Nonferrous Metals Society of China
www.tnmsc.cn

Interactive effects of porosity and microstructure on strength of 6063 aluminum alloy CMT MIX + Synchropulse welded joint

Qing-tao WANG[1,2], Xiao-nan WANG[1], Xia-ming CHEN[1], Peng-cheng HUAN[1,3], Qi-peng DONG[1], Qing-yu ZHANG[1], Hiromi NAGAUMI[1]

1. School of Iron and Steel, Soochow University, Suzhou 215002, China;
2. School of Mechanical and Transportation, Southwest Forestry University, Kunming 650224, China;
3. State Key Laboratory of Rolling and Automation, Northeastern University, Shenyang 110819, China

Received 5 March 2021; accepted 14 September 2021

Abstract: The porosity, pore size and softening of 6063 aluminum alloy CMT MIX + Synchropulse welded joint with different welding speeds were studied. The results show that with the increase of welding speed (from 55 to 65 cm/min), the porosity increases dramatically (from 0.1% to 3.9%) and large pores (341.1 μm) appear. The pore size distributions are mainly concentrated at 87.8 and 20.6 μm in the joints produced from weld speeds of 65 and 55 cm/min, respectively. The dissolution and transformation of the β'' phase in the base metal (BM) result in a significant softening of both the fusion zone and heat-affected zone, and the latter was more serious. The effects of welding speed on the average tensile strength of the full penetration welded joints are minor, which was about 155 MPa (67.4% that of the BM).

Key words: cold metal transfer; aluminum alloy; pore; microstructure; mechanical properties

1 Introduction

With the increasing pressures of energy conservation and environmental protection, lightweight of automobile has become one of the most effective ways to alleviate these problems [1]. Aluminum alloys have a wide range of applications in automotive manufacturing due to their low density (about 1/3 of steel), high strength, fair corrosion resistance and good capability plastic molding [2,3]. The joining of various components of the vehicle inevitably involves welding technologies, and the quality of welding directly influences the safety of the whole structure. The high thermal conductivity, high solidification rate, high thermal expansion coefficient and large solidification temperature range of aluminum alloy tend to produce a series of welding problems in the welding process of aluminum alloys, such as pores, thermal cracks, and softening [4,5]. Many studies were committed to solving these problems, and a series of new welding processes, such as cold metal transfer (CMT) [6] and sold state friction stir welding (FSW) [7], have been developed for welding aluminum alloys in recent years.

Cold metal transfer (CMT), invented by Fronius at the beginning of the 21st century, has become a significant technology in welding aluminum alloys due to its “cold” characteristics [8]. It is well known that the heat input is particularly critical for welding aluminum alloys. The softening and thermal deformation are more serious when the heat input is higher. However, the thickness of the aluminum alloy made for automotive structural parts has to be increased in certain cases so that the heat input (welding current) is increased accordingly. Many studies have shown that the

Corresponding author: Xiao-nan WANG, Tel/Fax: +86-512-67165621, E-mail: wxn@suda.edu.cn;
Qing-yu ZHANG, Tel/Fax: +86-512-67165621, E-mail: qingyu.zhang@suda.edu.cn
DOI: 10.1016/S1003-6326(22)65834-5

droplet transfer became unstable and resulted in welding defects when the welding current exceeded 100 A, leading to the traditional CMT process no longer suitable for welding aluminum alloy plate with thickness ≥2 mm [9]. Thus, the CMT + Pulse welding process was developed, which greatly increased the range of controllable heat input while maintaining the stability of droplet transfer, spatter-free and excellent metallurgical connection. PANG et al [10] compared CMT + Pulse process and traditional CMT process and revealed that the CMT + Pulse process generated higher heat input and had higher stability. CONG et al [11] found that CMT + Pulse process could significantly reduce the number and size of pores as compared with CMT process. However, the porosity, and softening of fusion zone (FZ) and heat-affected zone (HAZ) of the CMT + Pulse aluminum alloy welded joint were still observed. In our previous study [12], we found that the porosity and pore size of FZ with Si-rich welding wire (ER4047) were higher than those of Mg-rich welding wire (ER5183). The high porosity and large size pores reduced effective carrying area of the FZ and thus reduced the performance of the welded joints. However, when the porosity increased, it was not clear whether the welded joint fractured in the FZ or HAZ.

In addition, the CMT MIX + Synchropulse welding technology, as a new welding process, was rarely studied. There were few reports about the interactive effects of porosity, fusion zone softening and heat-affected zone softening on the strength of aluminum alloy weld joints, and the mechanism of the above three factors on the mechanical properties of welded joints was still unclear. Therefore, the CMT MIX + Synchropulse welding technology was used to weld 6063 aluminum alloys with the ER4047 filler. The relationship among the porosity, pore distribution, softening and mechanical properties was discussed. It was expected to provide a new idea for welding aluminum alloys and a necessary theoretical basis for further improving the service performance of aluminum alloy welded joints.

2 Experimental

2.1 Materials

The 6063-T6 aluminum alloy plates were used as base metals (BM) in this work, and the size of the welding sample was 150 mm × 100 mm × 3 mm. The chemical composition and mechanical properties of the BM are given in Tables 1 and 2, respectively. The welding wire used in this work was ER4047 (Al−Si) with a diameter of 1.2 mm, and its chemical composition is also given in Table 1. Figure 1 shows the microstructure of the BM. As shown in Fig. 1(a), the BM microstructure is a typical extruded microstructure with uneven grain size. There are two obvious second phases in the BM, namely, the white long strip phase and the black fine precipitated phase, as shown in Fig. 1(b). Furthermore, through the quantitative analysis of EDS, it is inferred that the white phase is AlFeSi phase and the black phase is β-Mg_2Si, which are derived from Table 3.

2.2 Methods

The welding machine used in the present work is TPS 500i produced by Fronius, Austria. The welding control system is a Kawasaki E series six-axis linkage robot. The surface of the sample was polished with $400^{\#}$ sandpaper, and cleaned with 99.9% alcohol before welding. The sample was then dried by cold air, and the welding experiment was completed within 30 min. The schematic diagram of the welding process is shown in Fig. 2. The type I butt welding (no gap) was adopted for welding. The protective gas is 99.99% argon, and the angle between the welding gun and the horizontal direction is 60°. The detailed welding parameters are given in Table 4. In this work, three welding speeds (55, 65 and 75 cm/min) were used to adjust the heat inputs.

In order to observe the microstructure and morphology of the welded joint, the cross sections of the metallographic samples of the welded joint were obtained by wire-electrode cutting. Then, the

Table 1 Chemical composition of 6063 aluminum alloy and ER4047 welding wire (wt.%)

Material	Mg	Si	Zn	Fe	Cu	Mn	Cr	Ti	Al
6063	0.525	0.412	0.002	0.09	0.002	0.002	0.001	0.014	Bal.
ER4047	<0.1	11.0−13.0	<0.2	<0.6	<0.3	<0.15	−	<0.15	Bal.

Table 2 Mechanical properties of 6063 aluminum alloy

Material	Yield strength/MPa	Tensile strength/MPa	Elongation/ %
6063	172.0	230.0	13.5

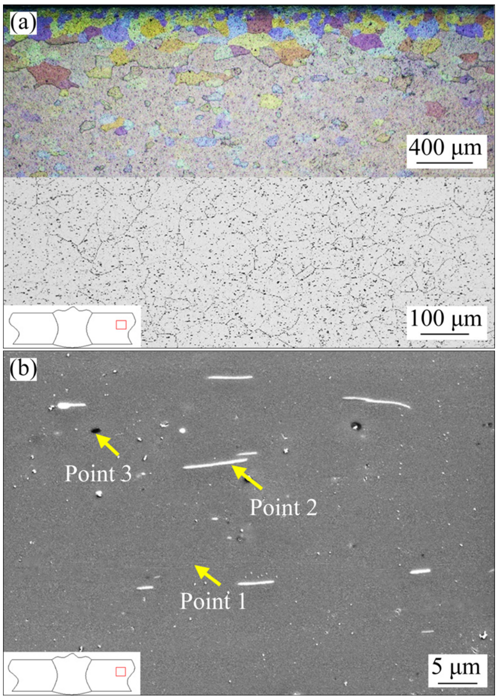

Fig. 1 Microstructures of 6063 aluminium alloy: (a) Anodic coating and metallographic image; (b) SEM image

Table 3 EDS analysis results of corresponding positions of base metal

Location	Content/at.%				Possible phase
	Al	Mg	Si	Fe	
Point 1	100	−	−	−	α(Al)
Point 2	87.41	0.55	6.63	5.40	AlFeSi
Point 3	72.18	7.51	10.35	0.04	β-Mg_2Si

samples were polished by different types of sandpaper and diamond polishing paste with particle size of 1.5 μm. Finally, SiO_2 suspension with particle size of 0.04 μm was used for fine polishing. The sample was corroded with Keller reagent (1 vol.% HF + 1.5 vol.% HCl + 2.5 vol.% HNO_3 + 95 vol.% H_2O). The corrosion time of the

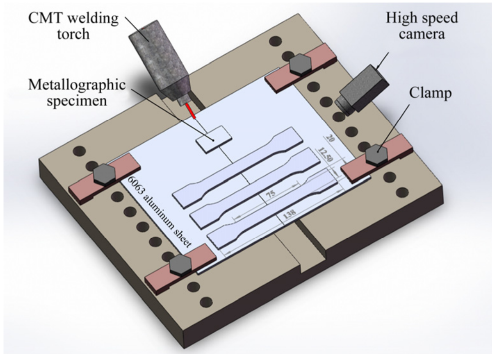

Fig. 2 Schematic of CMT tailoring, drawing and metallographic (unit: mm)

sample was 15−20 s. The anode coating was corroded by a mixed solution of sulfuric acid and phosphoric acid (38 vol.% sulfuric acid + 43 vol.% phosphoric acid + 19 vol.% water). The corrosion time and current were 120−150 s and 250−350 mA, respectively. The macroscopic morphology of the welded joint was observed on the SZX10 type stereoscopic microscope. The Image-Pro Plus (IPP) software was carried on the statistics of porosity and pore size. The macrostructure was observed and analyzed under the GX53 metallurgical microscope. The microstructure and the element distributions were observed by scanning electron microscope (SEM). The electron probe micro-analyzer (EPMA) was used to analyze the micro-zone composition of the welded joints. According to GB/T 4340.1—2009, automatic Vickers microhardness tester was used to measure the microhardness of the welding joint (the left and right intervals of the test points were 150 μm, and the upper and lower intervals were 0.6 mm). The load pressure was 1.96 N, and the loading time was 10.0 s.

The welded joint reinforcement was removed through mechanical processing for obtaining accurate mechanical properties of the welded joints. The details of tensile specimen size are shown in Fig. 2. In order to ensure the accuracy of the measured data, three tensile samples were made for the tensile test. The tensile test was completed on the universal testing machine according to the standard of GB/T 2651—2010, and the tensile

Table 4 Welding parameters for CMT MIX + Synchropulse process

Wire feeding speed/ ($m\cdot min^{-1}$)	High current time correction	Low energy period	Duty cycle/%	Peak arc length correction	Valley arc length correction
5.2	6.0	6.0	60	−3.0	−1.5

speed was 3.0 mm/min. After the tensile test, the fracture surface was washed by a ultrasonic cleaner with 99.9% alcohol, and then the fracture morphology of the tensile specimen was observed by SEM.

3 Results and discussion

3.1 Characteristics of porosity size and distribution of pores in fusion zone

The upper and lower surface views and cross-section morphologies of the welded joint with three different welding speeds are shown in Fig. 3. There are obvious fish scale patterns on the upper surface. The cross-section morphology presents obvious characteristics in different zones, which are respectively defined as fusion zone (FZ), partially molten zone (PMZ) and heat-affected zone (HAZ), respectively [13]. The cross-section morphology of the welded joint with three welding speeds is obviously different. When the welding speed is 75 cm/min, the welded joint is partially penetrated, and the width of the middle weld (LA2) is significantly smaller than that of the other two welding joints, as shown in Fig. 3(a). When the welding speed is decreased to 65 cm/min, the full penetration welded joint is obtained, and the widths of the middle (LA2) and bottom (LA3) weld (5.39 mm and 5.33 mm) increase significantly, as shown in Fig. 3(b). However, when the welding speed is reduced to 55 cm/min, the widths of the middle and bottom weld (5.87 mm and 5.94 mm) further increase, which can be seen in Fig. 3(c).

In addition, there are a large number of pores in the FZ with different welding speeds. Most of the pores present elliptical or oval shapes, which are typical metallurgical pore morphology features [12]. At the temperature of 600 °C and 1.013×10^{5} Pa, the solubility of hydrogen in pure aluminum drops from 6.9×10^{-3} to 3.6×10^{-4} mL/g, with a difference of about 20 times [14]. The sharp drop of hydrogen solubility leads to significant supersaturation of hydrogen in the molten pool, which cannot escape under the rapid cooling rate during welding process, and finally porosity is formed in the FZ, as shown in Fig. 3. The differences of pore size and porosity between the two kinds of full penetration welding joints are obvious. Further statistics and analysis of the pore size and porosity were carried out by using IPP software, and the results are shown in Fig. 4. It can be seen that when the welding speed is 65 cm/min, there are obvious macroscopic porosity

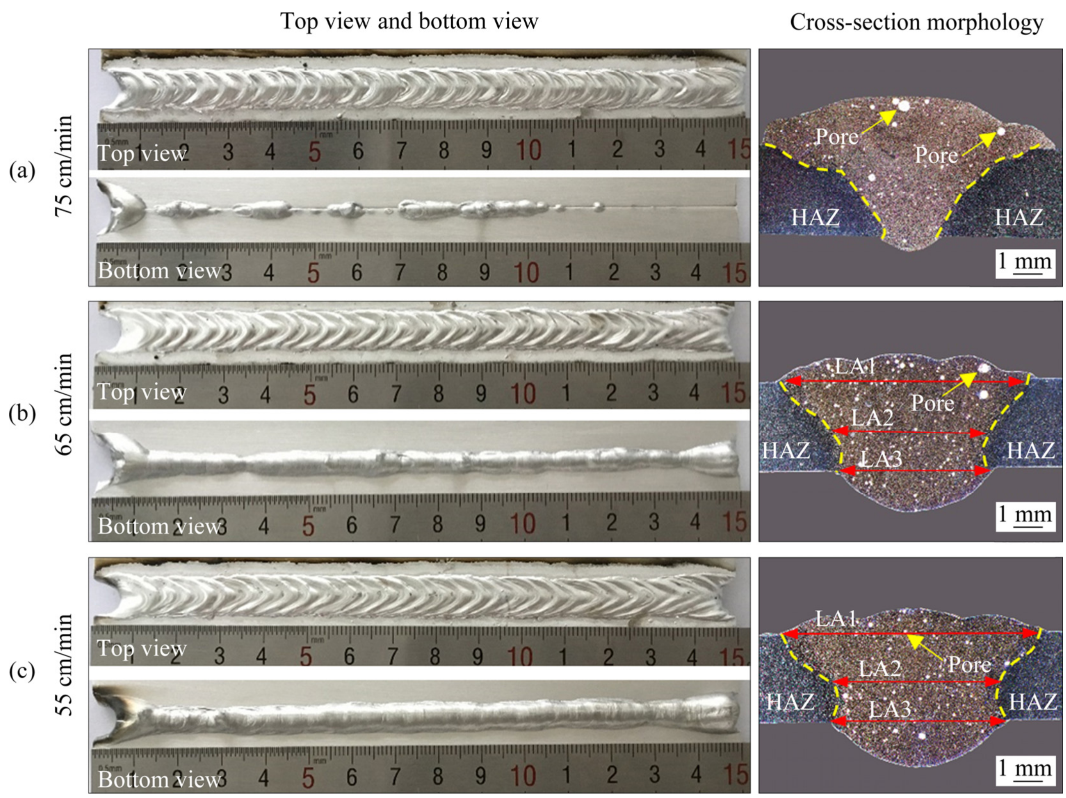

Fig. 3 Macroscopic morphology comparison of welded joints with different welding speeds: (a) 75 cm/min; (b) 65 cm/min; (c) 55 cm/min

(>200 μm) in the FZ. However, the largest pore size is only 60.1 μm at low welding speed (55 cm/min). From the distribution of the data points in Fig. 4, the pore size distributions are mainly concentrated at 20.6 μm (55 cm/min) and 87.8 μm (65 cm/min). Furthermore, it is found that as the welding speed is increased from 55 to 65 cm/min, the porosity has a significant increase (from 0.1% to 3.9%), which can be observed in Fig. 4(b).

The variations of FZ size characteristics, porosity and pore distribution are closely related to droplet transfer and the solidification of the molten pool. As compared to the traditional CMT, the heat input of CMT + Pulse process is mainly provided by the pulse stage.

Figure 5 shows the images of droplet transition in the pulse stage with the welding speed of 55 cm/min, taken by using a high-speed camera. As shown in Fig. 5(a), the welding wire is first melted by arc and a spherical droplet is formed at the end of the welding wire. The surface of the molten pool is obviously concave under the action of plasma

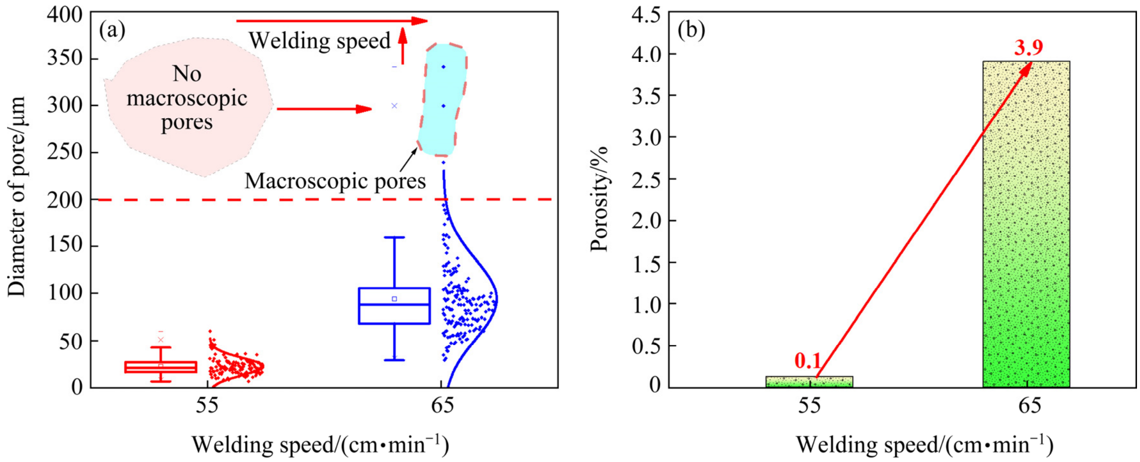

Fig. 4 Effects of welding speed on size and distribution of FZ pore (a) and porosity (b)

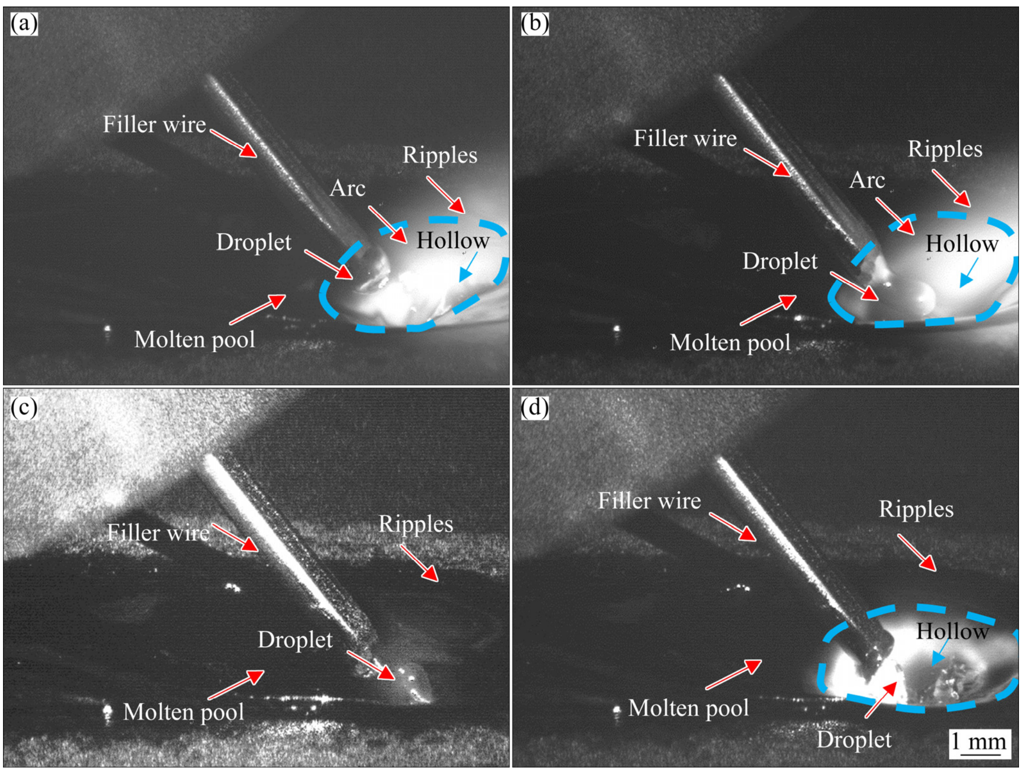

Fig. 5 Images of droplet transfer of welded joint taken by high-speed camera: (a) Arc striking stage; (b) Droplet starting to separate from welding wire; (c) Droplet completely detaching from welding wire; (d) Droplet completely entering into molten pool

fluid force. When the droplet diameter reaches a certain size (about 1.3 mm), the droplet falls off from the end of the welding wire under the actions of the electromagnetic contraction force and the gravity. Meanwhile, the molten pool is continuously affected by the plasma fluid force, and the width of the depression on the surface of the molten pool is increased. As shown in Figs. 5(b, c), the droplet falls off from the end of the welding wire and enters in the molten pool, while the surface of the molten pool is significantly rippled by the Marangoni flow. When the droplet completely enters in the molten pool, the molten pool in contact with the droplet fluctuates obviously under the action of droplet impact force. Meanwhile, the flow around the molten pool generates large ripples with the contact point at the center, as shown in Fig. 5(d). When the droplet enters in the molten pool, the molten pool in turn exerts a reverse force on the droplet, which causes the droplet to break. The final size difference of FZ with different welding speeds is mainly caused by the heat and convection of the molten pool. In general, with the decrease of welding speed, more welding wire can be melted per unit time and more droplets are formed. When more droplets enter the molten pool, the total heat of the molten pool increases, and the FZ depth and width are increased accordingly.

The formation and growth processes of pores are complicated, and there are many factors that affect the distribution and size of pores. Generally, when other conditions remain unchanged, the final size and distribution of pores are determined by the floating velocity and solidification speed of the molten pool [15]. The solidification rate of the molten pool has a great influence on pore. The higher the solidification rate is, the more difficult it is for pore to escape, so that the possibility of pore formation becomes greater [16]. When the pore floating velocity is larger than the molten pool solidification rate, the pore is easy to escape. Otherwise, the pore eventually remains in the molten pool. The low welding speed (high heat input) leads to prolonged solidification time of molten pool, which promotes more hydrogen to escape from the molten pool. In addition, due to the intensified flow in the molten pool in the CMT MIX + Synchropulse process, the pores are difficult to converge and grow, and the pores are dispersed in the FZ. The average size of the pores is small.

3.2 Microstructure and segregation of welded joint

When the welding wire and part of the BM are melted by arc to form a high temperature molten pool, the heat is conducted to the other base metal nearby and then solidification occurs. This process inevitably causes the BM to undergo a heat treatment process at different peak temperatures. Therefore, at different distances from the weld center, the microstructure of each area in the welded joint may change significantly [5,12]. The rules of microstructure and element segregation of the welded joint with different heat inputs are similar, and the welding joint with welding speed of 55 cm/min is taken as an example to study the rule of microstructure and element segregation of full penetration welded joint [17].

Figure 6 shows the microstructure and metallographic diagram of different areas of the welded joint with a welding speed of 55 cm/min. Figure 6(a) shows the FZ center microstructure after anodic coating, which is composed of a large number of equiaxed grains. Figure 6(b) shows the metallographic diagram of FZ center microstructure after being corroded by Keller's reagent, which is composed of a gray colored α(Al) matrix and

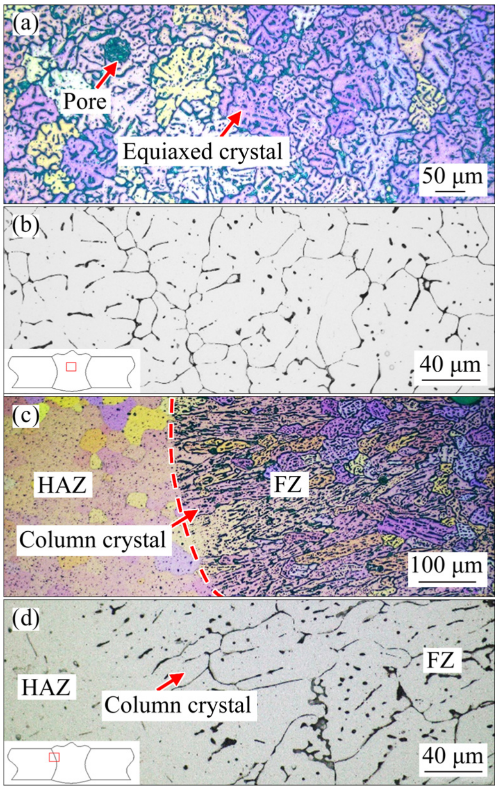

Fig. 6 Microstructures of FZ and PMZ with welding speed of 55 cm/min: (a, b) FZ; (c, d) PMZ

intermittent dendrites. The PMZ microstructure consists of obvious columnar crystals, as shown in Figs. 6(c, d). The variation of grain morphology in different regions of welded joint is related to the component supercooling. At the beginning of solidification crystallization, the temperature gradient near PMZ is large and the supercooling of the components is low. With the solidification process going on, the concentration of liquid solute in the front of crystallization is increased and the supercooling zone is also increased, which causes the crystal in the molten pool to change from columnar crystal to equiaxial crystal [18,19].

The distribution of the main elements in the FZ is shown in Fig. 7. Significant segregations of elements Si and Mg are observed in the FZ. During solidification process, Mg and Si elements are rejected into the liquid phase, which causes the solute concentration in the liquid phase to enrich and segregations of Si and Mg finally are formed at the end of solidification [20]. Continuous eutectic Si exists in dendrites around α(Al) in the FZ, as shown in Figs. 7(b, c). In addition, Mg and Si elements have some overlap areas, which is presumed to be the β-Mg_2Si phase, as shown in Figs. 7(c, e). In order to further determine the precipitation phase in the FZ, EDS quantitative analysis was performed, as shown in Fig. 8. The contents of three typical regions (A, B, and C) are given in Table 5. According to the EDS results, the white elongated needle-like phase in Zone A is the AlFeSi phase, and the black spherical precipitate in Zone B is β-Mg_2Si phase. During the welding process, the welding wire and part of the BM are melted by arc and the molten pool is formed. The temperature of the molten pool already exceeds the dissolution temperature of the β' and β'' phases, which causes the nano-scale β' and β'' phases of the BM to completely dissolve and then precipitate out in the form of the large β-Mg_2Si phase during the subsequent cooling process. The β-Mg_2Si phase is completely noncoherent with the α(Al) matrix and has little strengthening effect, resulting in a significant softening of FZ.

3.3 Microhardness and tensile properties of welded joints

Figure 9 shows the distribution of micro-hardness on the two-dimensional surface of the welded joint. As shown in Fig. 9, the microhardness of FZ and HAZ is significantly lower than that of the base material, and obvious softening appears in the welding joint (the microhardness of the base material is about HV 75). The softening of HAZ is the most serious, and the minimum microhardness of the welded joint appears in the HAZ near the BM side (only 64% of the base metal), as shown in Fig. 9(a). With the decrease of welding speed, the width of HAZ increases (from 7.7 mm to 10.0 mm). In order to understand the microhardness distribution

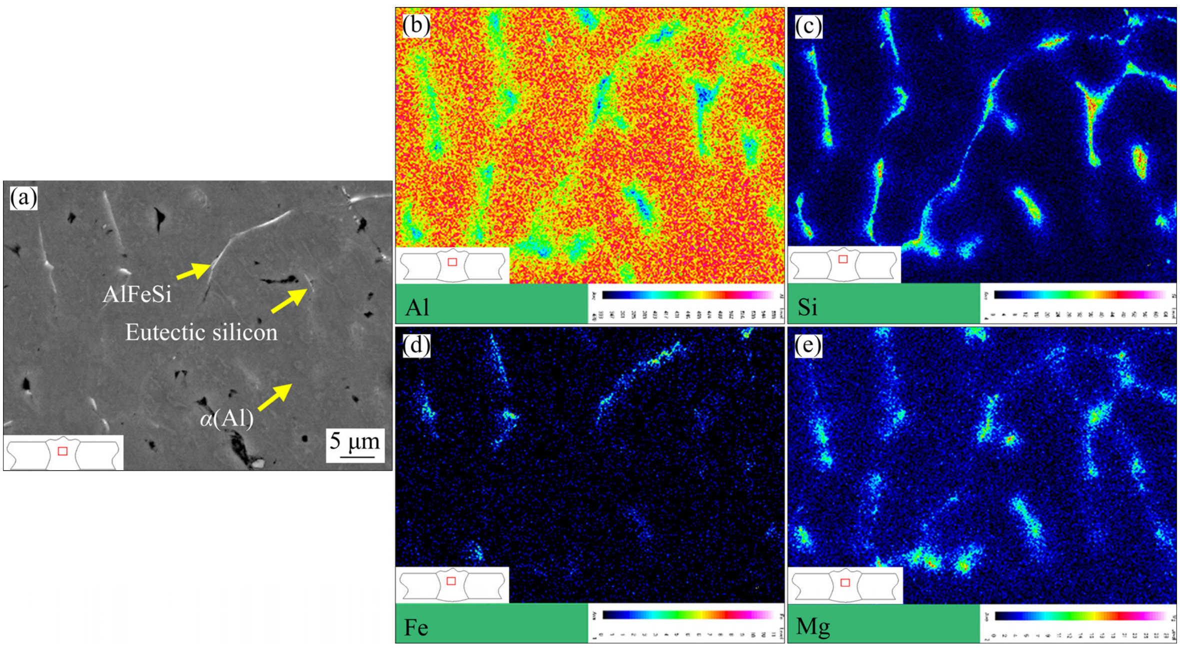

Fig. 7 EPMA results of FZ with welding speed of 55 cm/min: (a) SEM image; (b) Al; (c) Si; (d) Fe; (e) Mg

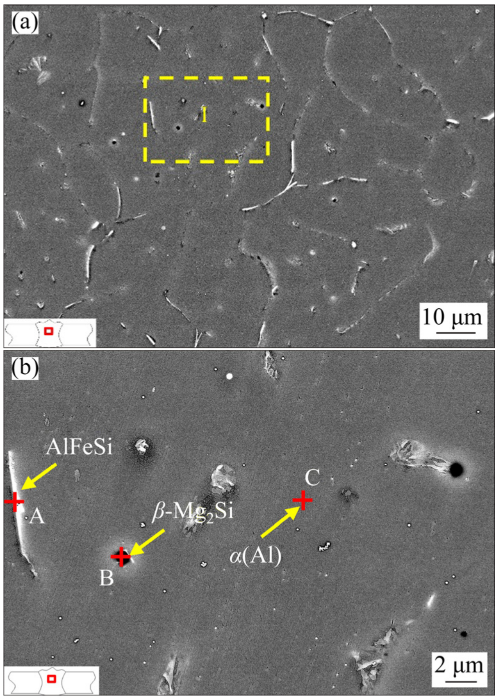

Fig. 8 SEM images of FZ with welding speed of 55 cm/min

Table 5 EDS quantitative analysis results of different positions of FZ with welding speed of 55 cm/min

Zone in Fig. 8	Content/at.%				Possible phase
	Al	Mg	Si	Fe	
A	87.6	0.7	8.2	3.5	AlFeSi
B	83.6	1.9	13.1	1.4	β-Mg_2Si
C	98.77	0.13	1.06	0.04	α(Al)

law of the welded joint, the three-dimensional micro-hardness distribution map of the welded joint with the 55 cm/min welding speed is drawn in Fig. 9(b).

Three-dimensional microhardness distribution map shows that the FZ and HAZ are obviously softened. In addition, there are two obvious peaks in PMZ and an obvious trough in the overaging zone of the HAZ. The material used in this study is 6063-T6 aluminum alloy (Al−Mg−Si). The precipitation sequence of the Al−Mg−Si aluminum alloys is SSSS → GP (spherical) → β'' (needle) → β' (rod) → β (Mg_2Si) [21]. The transformation law of the main strengthening phase (β'') in the BM during the welding thermal cycle is the fundamental reason for softening. The results of relevant literatures showed that the β'' (coherent relationship with matrix) and β' (semi-coherent relationship with

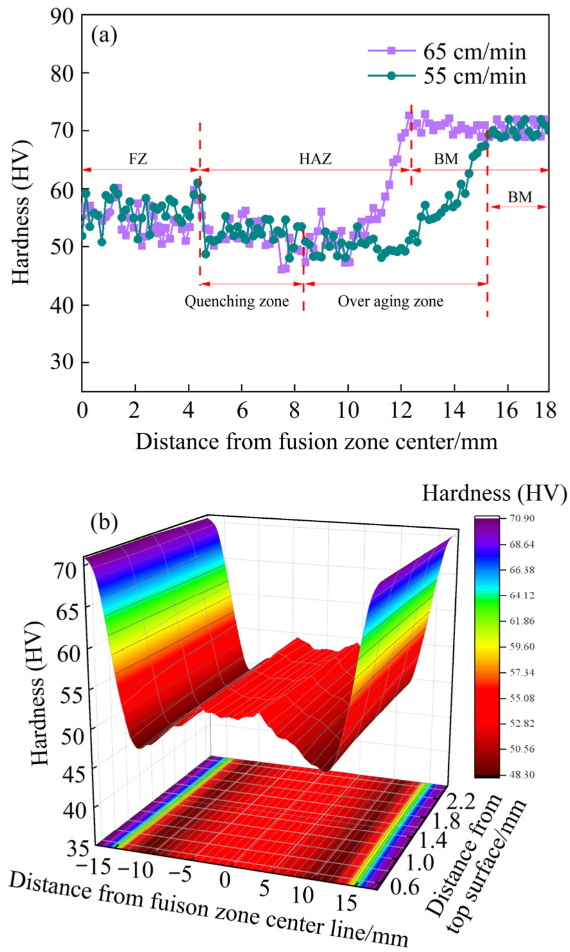

Fig. 9 Two-dimensional microhardness distribution of full penetration welded joint (a) and three-dimensional distribution of welded joint with welding speed of 55 cm/min (b)

matrix) phases play the main roles in strengthening, while β-Mg_2Si is completely incoherent with the matrix and has almost no strengthening effect on the matrix [22]. VARGAS et al [23] studied the transition temperature range of β'', β' and β phases, which were 160−240, 240−380 and 380−480 °C, respectively. The peak temperature in the welding process has far exceeded the transformation temperature of strengthening phase. In the FZ, the welding wire and part of the base metal are melted rapidly by electric arc and the molten pool is formed. The β'' phase completely dissolves in molten pool and then precipitates in the form of β-Mg_2Si phase during the subsequent cooling process [24]. This result has been confirmed in Section 3.2. In addition, a certain extent of element Mg in the base metal is burned in the welding process, which also leads to the softening of FZ. Therefore, the precipitation of β-Mg_2Si phase and the burning loss of Mg element contribute to the softening of FZ. The increase of microhardness in the PMZ is due to the fact that the position is close to the molten pool, and the heating and cooling speeds are very fast during the welding process, which is equivalent to the effect of solution quenching [25,26]. The peak temperature of HAZ also exceeds the dissolution temperature of β'' phase. The partial or complete dissolution of β'' phase occurs during the welding thermal cycle, and the transformation of β'' phase to β' phase and β phase results in the sharp decrease of microhardness of HAZ. This result is consistent with the work of YAN et al [27], ZHANG et al [28] and YAN et al [29].

Figure 10 shows the morphology and engineering stress−strain curves of tensile test samples of full penetration welded joints with different welding speeds. It can be seen from Fig. 10(a) that the welded joints are all fractured in HAZ (besides the partial penetrated welded joint). The average tensile strength of the full penetration welded joints with different welding speed is equivalent, which is about 155 MPa (67.4% that of the BM), as shown in Fig. 10(b). The tensile fracture surfaces of the two full penetration welded

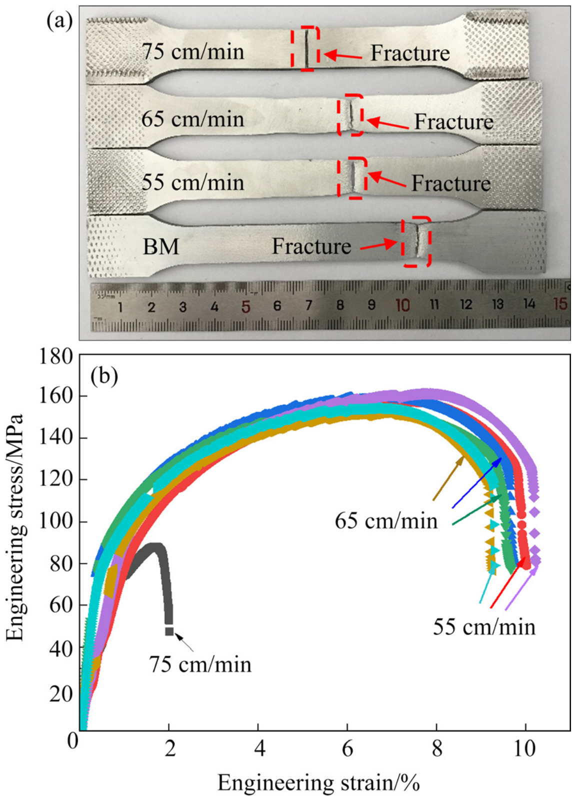

Fig. 10 Morphologies of tensile testing samples (a) and engineering stress−strain curves (b)

joints are further characterized, as shown in Fig. 11. The fracture surface of tensile specimens with different welding speeds present obvious dimples, which denote obvious ductile fracture characteristics. There are two main reasons for the fracture of full penetration welded joint in HAZ rather than in the FZ. The first reason is that the softening of HAZ is more serious than that of FZ. On the other hand, although there are a larger number of pores in the FZ, especially in the case of high welding speed, the pores are uniformly distributed and there are no continuous pores with dense distribution. These indicate that although there are softening and porosity in the FZ, it is not the weakest area of the whole welded joint. The softening degree of HAZ is the main factor affecting the mechanical properties of the 6063 aluminum alloy CMT MIX + Synchropulse welded joints.

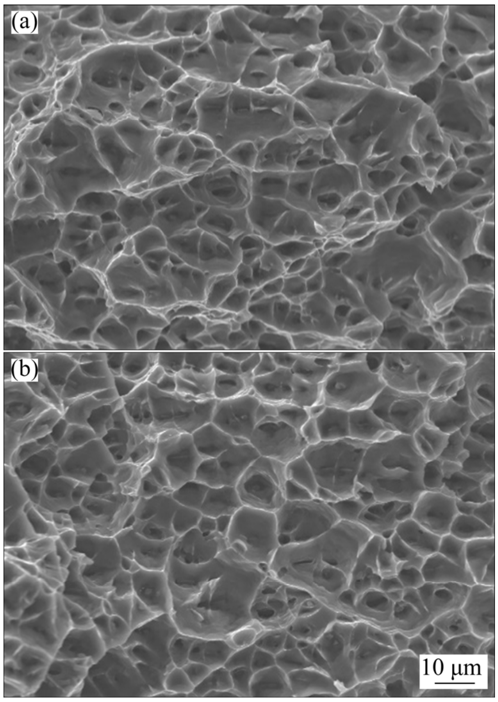

Fig. 11 SEM morphologies of tensile fracture of welded joints with different welding speeds: (a) 65 cm/min; (b) 55 cm/min

4 Conclusions

(1) With the increase of welding speed, the porosity of weld increases rapidly (from 0.1% to 3.9%) and large pores (341.1 μm) are formed. The pore size is about 87.8 and 20.6 μm in the joints produced using a weld speed of 65 and 55 cm/min,

respectively.

(2) Significant segregation of elements Si and Mg are observed in the FZ with different welding speeds. The dissolution and transformation of β'' phase result in obvious softening of FZ and HAZ. The average tensile strength of the full penetration welded joints with different welding speeds are equivalent (about 155 MPa, 67.4% that of the BM).

(4) The pores distribute uniformly in FZ and the softening degree is lower than that of HAZ, which implies that FZ is not the weakest zone in the whole welded joint. The softening of the HAZ is the main factor affecting the mechanical properties of the welded joints.

Acknowledgments

This work was financially supported by the Major Program of the National Natural Science Foundation of China (No. U1864209) and the "Qinglan" Project of Jiangsu Province, China.

References

[1] WANG X N, SUN Q, ZHENG Z, DI H S. Microstructure and fracture behavior of laser welded joints of DP steels with different heat inputs [J]. Materials Science and Engineering A, 2017, 699: 18−25.

[2] İPEKOĞLU G, ÇAM G. Effects of initial temper condition and postweld heat treatment on the properties of dissimilar friction-stir-welded joints between AA7075 and AA6061 aluminum alloys [J]. Metallurgical and Materials Transactions A, 2014, 45A: 3074−3087.

[3] XU Wei-feng, MA Jun, WANG Miao, LU Hong-jian, LUO Yu-xuan. Effect of cooling conditions on corrosion resistance of friction stir welded 2219-T62 aluminum alloy thick plate joint [J]. Transactions of Nonferrous Metals Society of China, 2020, 30(6): 1491−1499.

[4] ÇAM G, M. KOÇAK M. Microstructural and mechanical characterization of electron beam welded Al-alloy 7020 [J]. Journal of Materials Science, 2007, 42(17): 7154−7161.

[5] PAKDIL M, ÇAM G, KOÇAK M, ERIM S. Microstructural and mechanical characterization of laser beam welded AA6056 Al-alloy [J]. Materials Science and Engineering A, 2011, 528: 7350−7356.

[6] TIAN Y B, SHEN J Q, HU S S, WANG Z J, GOU J. Effects of ultrasonic vibration in the CMT process on welded joints of Al alloy [J]. Journal of Materials Processing Technology, 2018, 259: 282−291.

[7] KASHAEV N, VENTZKE V, ÇAM G. Prospects of laser beam welding and friction stir welding processes for aluminum airframe structural applications [J]. Journal of Manufacturing Processes, 2018, 36: 571−600.

[8] GUNGOR B, KALUC E, TABAN E, SIK A. Mechanical and microstructural properties of robotic cold metal transfer (CMT) welded 5083-H111 and 6082-T651 aluminum alloys [J]. Materials & Design, 2014, 54: 207−211.

[9] ZHANG H T, FENG J C, HE P, ZHANG B B, CHEN J M, WANG L. The arc characteristics and metal transfer behaviour of cold metal transfer and its use in joining aluminium to zinc-coated steel [J]. Materials Science and Engineering A, 2009, 499: 111−113.

[10] PANG J, HU S S, SHEN J Q, WANG P, LIANG Y. Arc characteristics and metal transfer behavior of CMT + P welding process [J]. Journal of Materials Processing Technology, 2016, 238: 212−217.

[11] CONG B, DING J, WILLIAMS S. Effect of arc mode in cold metal transfer process on porosity of additively manufactured Al−6.3%Cu alloy [J]. International Journal of Advanced Manufacturing Technology, 2015, 76(9−12): 1593−1606.

[12] HUAN P C, WANG X N, ZHANG J, HU Z R, CHEN W G, NAGAUMI H M, DI H S. Effect of wire composition on microstructure and properties of 6063 aluminium alloy hybrid synchronous pulse CMT welded joints [J]. Materials Science and Engineering A, 2020, 790: 139713.

[13] BAI R X, WEI Y P, LEI Z K, JIANG H, TAO W, YAN C, LI X L. Local zone-wise elastic-plastic constitutive parameters of Laser-welded aluminium alloy 6061 using digital image correlation [J]. Optics and Lasers in Engineering, 2018, 101: 28−34.

[14] DEWAN M W, WAHAB M A, OKEIL A M. Influence of weld defects and postweld heat treatment of gas tungsten arc-welded AA-6061-T651 aluminum alloy [J]. Journal of Manufacturing Science and Engineering, 2015, 137(5): 051027.

[15] HUANG J L, WARNKEN N, GEBELIN J C, STRANGWOOD M, REED R C. On the mechanism of porosity formation during welding of titanium alloys [J]. Acta Materialia, 2012, 60: 3215−3225.

[16] LIANG Y, HU S, SHEN J Q, ZHANG H, WANG P. Geometrical and microstructural characteristics of the TIG-CMT hybrid welding in 6061 aluminum alloy cladding [J]. Journal of Materials Processing Technology, 2017, 239: 18−30.

[17] MIN D, SHEN J, LAI S Q, CHEN J. Effect of heat input on the microstructure and mechanical properties of tungsten inert gas arc butt-welded AZ61 magnesium alloy plates [J]. Materials Characterization, 2009, 60: 1583−1590.

[18] CHU Q L, BAI R X, JIAN H G, LEI Z K, HU N, YAN C. Microstructure, texture and mechanical properties of 6061 aluminum laser beam welded joints [J]. Materials Characterization, 2018, 137: 269−276.

[19] LIU J, ZHU H Y, Li Z, CUI W F, SHI Y. Effect of ultrasonic power on porosity, microstructure, mechanical properties of the aluminum alloy joint by ultrasonic assisted laser-MIG hybrid welding [J]. Optics & Laser Technology, 2019, 119: 105619.

[20] NIE F H, DONG H G, CHEN S, LI P, WANG L Y, ZHAO Z X, LI X T, ZHANG H. Microstructure and mechanical properties of pulse MIG welded 6061/A356 aluminum alloy dissimilar butt joints [J]. Journal of Materials Science & Technology, 2018, 34(3): 551−560.

[21] HUIS M A V, CHEN J H, ZANDBERGEN H W, SLUITER

M H F. Phase stability and structural relations of nanometer-sized, matrix-embedded precipitate phases in Al–Mg–Si alloys in the late stages of evolution [J]. Acta Materialia, 2006, 54: 2945−2955.

[22] MYHR O R, GRONG Ø, FJAER H G, MARIOARA C D. Modelling of the microstructure and strength evolution in Al−Mg−Si alloys during multistage thermal processing [J]. Acta Materialia, 2004, 52: 4997−5008.

[23] VARGAS J A, TORRES J E, PACHECO J A, HERNANDEZ R J. Analysis of heat input effect on the mechanical properties of Al-6061-T6 alloy weld joints [J]. Materials & Design, 2013, 52: 556−564.

[24] PICKIN C G, YOUNG K. Evaluation of cold metal transfer (CMT) process for welding aluminium alloy [J]. Science & Technology of Welding & Joining, 2006, 11(5): 583−585.

[25] LEFEBVRE F, GANGULY S, SINCLAIR I. Micromechanical aspects of fatigue in a MIG welded aluminium airframe alloy: Part 1. Microstructural characterization [J]. Materials Science and Engineering A, 2005, 397: 338−345.

[26] MIAO W F, LAUGHLIN D E. Precipitation hardening in aluminum alloy 6022 [J]. Scripta Materialia, 1999, 40: 873−878.

[27] YAN S H, CHEN H, ZHU Z T, GOU G Q. Hybrid laser-metal inert gas welding of Al−Mg−Si alloy joints: microstructure and mechanical properties [J]. Materials & Design, 2014, 61: 160−167.

[28] ZHANG W K, HE H, XU C C, YU W Y, LI L X. Precipitates dissolution, phase transformation, and re-precipitation-induced hardness variation in 6082-T6 alloy during MIG welding and subsequent baking [J]. JOM: The Journal of the Minerals, Metals & Materials Society, 2019, 71: 2711−2720.

[29] YAN S H, XING B B, ZHOU H Y, XIAO Y, QIN Q H, CHEN H. Effect of filling materials on the microstructure and properties of hybrid laser welded Al−Mg−Si alloys joints [J]. Materials Characterization, 2018, 144: 205−218.

气孔和显微组织对 6063 铝合金双脉冲耦合 CMT 焊接接头强度的协同影响

王清涛 [1,2]，王晓南 [1]，陈夏明 [1]，环鹏程 [1,3]，董其鹏 [1]，张庆宇 [1]，Hiromi NAGAUMI [1]

1. 苏州大学 沙钢钢铁学院，苏州 215002；
2. 西南林业大学 机械与交通学院，昆明 650224；
3. 东北大学 轧制及连轧自动化国家重点实验室，沈阳 110819

摘 要：研究不同焊接速度下 6063 铝合金“CMT MIX+ Synchropulse”焊接接头的焊缝气孔率、气孔尺寸以及焊缝和热影响区的软化。结果表明，随着焊接速度从 55 cm/min 提高到 65 cm/min，焊缝气孔率从 0.1%增加至 3.9%，且出现大尺寸气孔(341.1 μm)。65 cm/min 时焊缝气孔尺寸主要集中分布在 87.8 μm，而 55 cm/min 时的气孔尺寸主要集中分布在 20.6 μm。基材中 β''相溶解与转变导致焊缝和热影响区均出现明显的软化，热影响区的软化更为严重。不同焊接速度焊接接头平均抗拉强度相当，约 155 MPa(达到母材的 67.4%)。

关键词：冷金属过渡；铝合金；气孔；显微组织；力学性能

(Edited by Bing YANG)